SCIENCE ADVANCES | RESEARCH ARTICLE

ATMOSPHERIC SCIENCE

Climate sensitivity and relative humidity changes in global storm-resolving model simulations of climate change

Timothy M. Merlis[1]*, Kai-Yuan Cheng[1], Ilai Guendelman[1], Lucas Harris[2], Christopher S. Bretherton[3], Maximilien Bolot[1], Linjiong Zhou[1], Alex Kaltenbaugh[2], Spencer K. Clark[2,3], Gabriel A. Vecchi[1], Stephan Fueglistaler[1]

Copyright © 2024 The Authors, some rights reserved; exclusive licensee American Association for the Advancement of Science. No claim to original U.S. Government Works. Distributed under a Creative Commons Attribution NonCommercial License 4.0 (CC BY-NC).

The climate simulation frontier of a global storm-resolving model (GSRM; or *k*-scale model because of its kilometer-scale horizontal resolution) is deployed for climate change simulations. The climate sensitivity, effective radiative forcing, and relative humidity changes are assessed in multiyear atmospheric GSRM simulations with perturbed sea-surface temperatures and/or carbon dioxide concentrations. Our comparisons to conventional climate model results can build confidence in the existing climate models or highlight important areas for additional research. This GSRM's climate sensitivity is within the range of conventional climate models, although on the lower end as the result of neutral, rather than amplifying, shortwave feedbacks. Its radiative forcing from carbon dioxide is higher than conventional climate models, and this arises from a bias in climatological clouds and an explicitly simulated high-cloud adjustment. Last, the pattern and magnitude of relative humidity changes, simulated with greater fidelity via explicitly resolving convection, are notably similar to conventional climate models.

INTRODUCTION

The use of kilometer-scale (*k*-scale) global storm-resolving models (GSRMs) on global domains has emerged as a promising frontier of modeling Earth's atmosphere (*1*, *2*). The implications of this new class of models for climate change are in their nascent stage (*3*–*8*). GSRMs are being developed by numerous modeling centers, and several models in this class have participated in a recent intercomparison ("DYAMOND") of 40-day integrations initialized from analyzed atmospheric states (*9*). Using initialized integrations is desirable in that it facilitates comparison to detailed Earth observations of particular weather statistics, model assessment akin to numerical weather prediction evaluation. A central motivation for the push to *k*-scale global climate models (GCMs) is, however, addressing uncertainty in climate model formulation by explicitly resolving more of the interactions between the atmospheric flow and the phase change of water vapor. These interactions are, of course, responsible for clouds and precipitation and are intimately tied to the planetary radiation balance (*10*, *11*). GSRMs explicitly simulate aspects of deep moist convection without using sub–grid scale parameterization. Ambitious research visions and descriptions of requisite resources for this frontier of climate prediction have been recently described (*12*, *13*).

Here, we offer an overview of key aspects of global climate change in four distinct 2-year-long free-running GSRM simulations with the Geophysical Fluid Dynamics Laboratory's (GFDL) eXperimental System for High-resolution prediction on Earth-to-Local Domains [X-SHiELD; with ≈3.25 km horizontal resolution and no deep convection scheme (*5*, *14*); Materials and Methods]: A control, one with a uniform 4-K sea-surface temperature (SST) warming, one with an increased CO_2 concentration, and one with both. These perturbation simulations have a long history in atmospheric model simulations of climate change and can be used to assess climate sensitivity (*15*, *16*) and radiative forcing (*17*, *18*).

Figure 1 shows the instantaneous distribution of column-integrated cloud ice and liquid water over the Americas for the control simulation's 8 August 2020 (left). This provides a vivid illustration of the detailed flows that are explicitly simulated, from the large-scale fronts sweeping across much of the southern hemisphere midlatitudes and the sharp East Pacific ITCZ to the *k*-scale convection from Mexico to South America. This type of imagery is evocative, and we are further interested in the aggregate effect of these small-scale features on the global-scale variables that control the climate response to external forcing. We see a similar image for the global warming simulation (Fig. 1, right), noting that one cannot readily discern the effect of climate change from the instantaneous cloud morphology. Our climate change motivation naturally mandates a systematic investigation of the averaged state of these simulated atmospheres. Here, we focus on the top-of-atmosphere (TOA) energy balance and some of the key factors underlying its response to climate change.

Given that we are analyzing long GSRM simulations and extracting their climate change responses, a natural point of comparison is conventional GCMs that use parameterizations for unresolved moist convection. These have been the dominant means of quantitative future climate projections from the inception of the Intergovernmental Panel on Climate Change Assessment Reports to the present Coupled Model Intercomparison Project Phase 6 (CMIP6) simulations. To the extent that the GSRM simulations are within the range of conventional climate models, it suggests that the net effect of the unresolved-but-parameterized processes on the mean climate is consistent with *k*-scale models that simulate more of the atmospheric flow. This possibility would be reassuring from the perspective of the continued relevance of existing climate change assessments based on conventional climate models. To the extent that the GSRM simulations are outside the range of conventional climate models, it suggests important areas of future inquiry. This may indicate that

---

[1]Program in Atmospheric and Oceanic Sciences, Princeton University, 300 Forrestal Road, Princeton, NJ 08540, USA. [2]Geophysical Fluid Dynamics Laboratory, NOAA, Princeton, NJ 08540, USA. [3]Allen Institute for Artificial Intelligence, Seattle, WA 98109, USA.
*Corresponding author. Email: tmerlis@princeton.edu

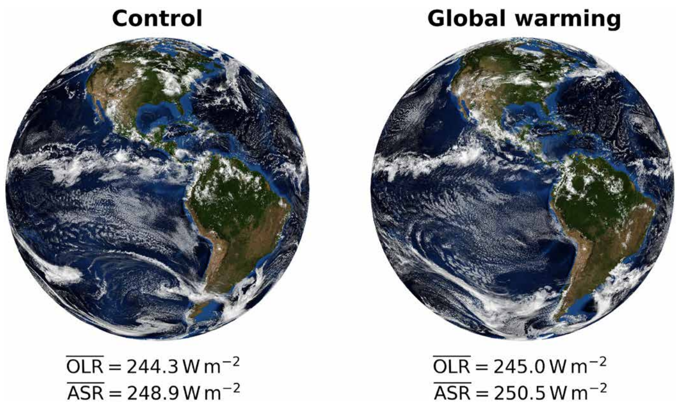
Control
Global warming
$\overline{\text{OLR}} = 244.3\ \text{W m}^{-2}$
$\overline{\text{ASR}} = 248.9\ \text{W m}^{-2}$
$\overline{\text{OLR}} = 245.0\ \text{W m}^{-2}$
$\overline{\text{ASR}} = 250.5\ \text{W m}^{-2}$

Fig. 1. Instantaneous simulated cloud liquid and ice water paths for 8 August 2020 in control and global warming (4K SST warming with increased CO_2 concentration) X-SHiELD GSRM simulations. The global- and time-mean outgoing longwave radiation (OLR) and absorbed shortwave radiation (ASR) components of the TOA net radiation over the two simulated years are indicated below the instantaneous images.

improvements can be made in the formulation of GSRMs (e.g., if there are biases with respect to observations) or it may suggest that parameterizations in conventional climate models distort the simulated climate changes in a way that must be revisited with better resolved atmospheric simulations. It is, therefore, a high priority to undertake the comparison of GSRM simulations of climate change relative to existing climate model results. This is complementary to the important goal of examining previously unresolved phenomena, such as the changes in extreme convective vertical velocities with warming (*5*).

RESULTS

The time-mean components of global-mean TOA net radiation, the outgoing longwave radiation (OLR) and absorbed shortwave radiation (ASR), are shown for the control simulation in Fig. 1 (left). Here and throughout, we use the simulated calendar years 2020 and 2021. Compared to satellite estimates from CERES EBAF (*19*), X-SHiELD has positive global-mean biases of about 7 W m^{-2} for ASR and about 4 W m^{-2} for OLR. Note that this X-SHiELD configuration has not been extensively optimized against the TOA observations, as this is computationally infeasible for this length of integration.

The global-mean TOA components for the global warming simulation (increased SST with increased CO_2) have increased OLR (+0.7 W m^{-2}) and ASR (+1.6 W m^{-2}, right versus left of Fig. 1). CO_2 is a greenhouse gas that increases the planet's net TOA radiation (primarily by decreasing OLR) and this is offset by stabilizing temperature-dependent feedbacks. The change in net radiation (+0.9 W m^{-2}) indicates additional energy imbalance, despite our desire to obtain a similar degree by tailoring the perturbation CO_2 concentration (imposing a ≈3.1× increase compared to the control). However, the assumption of linear superposition between the isolated roles of warming and CO_2 forcing holds well, as our forcing-feedback analysis will show.

This set of simulations can define the two key components of the canonical climate feedback analysis. The changes in the global-mean TOA energy balance are decomposed into the radiative forcing $\mathscr{F}$ and the climate feedback parameter λ. At equilibrium, there is no change in net radiation ΔN and

$$\Delta N = 0 = \mathscr{F} + \lambda \Delta T_s \qquad (1)$$

where all quantities are global means and the sign convention is that a stable climate feedback parameter is negative. That is, a positive forcing $\mathscr{F} > 0$ from an increased CO_2 concentration provokes a warming $\Delta T_s > 0$ for the energy balance to re-equilibrate.

The change in TOA net radiation for the simulation with increased CO_2 and unchanged SST defines the effective radiative forcing (ERF). This is the typical way of specifying $\mathscr{F}$ in Eq. 1. The ERF is also referred to as the troposphere-adjusted forcing (*17*, *18*). It allows for changes in the stratospheric temperatures driven by the CO_2 concentration, rather than the surface warming, and analogous CO_2 concentration-dependent tropospheric adjustments (*20*). Since the CO_2 concentration changes differ in X-SHiELD and the corresponding CMIP6 experiment, we assume a logarithmic scaling in CO_2 concentration to estimate X-SHiELD's $4 \times CO_2$ radiative forcing.

The ERF is 9.0 W m^{-2} in X-SHiELD (left side of Fig. 2A). The CMIP6 ERF ensemble mean of 7.9 W m^{-2} is smaller than X-SHiELD's. Figure 2 shows both individual CMIP6 models (colored circles) and an estimate of their distribution (gray lines). X-SHiELD is above the top of the range of the multimodel distribution of ERF (Fig. 2A). For the CMIP6 simulations, ERF assessed using time-means over 2 (versus 30) simulated years changes by ≈±0.3 W m^{-2} (fig. S1). The two individual years of X-SHiELD ERF differ by 0.1 W m^{-2}, suggesting that the difference relative to CMIP6 is not related to the limited time sampling.

The longwave (LW) component of the ERF, the reduction in OLR, is 7.3 W m^{-2} in X-SHiELD. This is larger than the CMIP6 ensemble mean (6.3 W m^{-2}), although there is one GCM that has comparably large LW forcing (right side of Fig. 2A). The shortwave (SW) component of the ERF is +1.8 W m^{-2} in X-SHiELD, comparable to the ensemble-mean of CMIP6 models, +1.7 W m^{-2}, which has larger variations in 2-year averages than the LW component (fig. S1). The CMIP6 models are colored by their ERF, which can be used to infer the extent to which LW and SW components produce variation across models. Broadly, the LW dominates the ERF and the SW on average increases it but can decrease it in some models.

X-SHiELD's larger LW forcing is related to the climatological high cloud distribution. Its cloud-top temperatures are biased warm (i.e., lower in altitude; fig. S2), so additional CO_2 causes a larger reduction in OLR. A high-cloud adjustment also contributes to the forcing: CO_2 increases the cloud fraction and ice concentration above the control cloud top and decreases them below (fig. S3). This increases the LW forcing by lifting cloud tops to emit from colder temperatures. This high-cloud adjustment is an intriguing response given the *k*-scale model simulates the deep convection responsible for these clouds and its LW ERF differs from GCM behavior (*18*). Previous GSRM analyses have found increased high clouds in response to SST warming (*3*, *21*), but this is the first example of a similar cloud response to increased CO_2 without any SST change.

The Cess climate sensitivity is determined by the feedback parameter computed from the difference in global-mean net radiation in response to the uniform SST perturbation with unchanged CO_2 concentration: $\lambda = \Delta N / \Delta T_s$, where the global-mean surface air temperature change ΔT_s includes enhanced land warming. The Cess sensitivity can be expressed in terms of a feedback parameter λ of

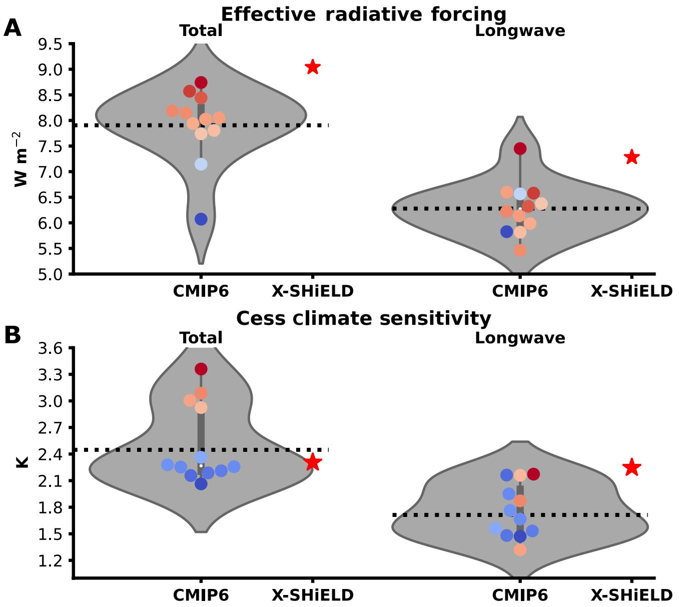

Fig. 2. Forcing-feedback decomposition of changes in global-mean TOA net radiation assessed in X-SHiELD GSRM simulations compared to CMIP6 simulations. (**A**) Effective radiative forcing (ERF) for X-SHiELD (red star) versus CMIP6 models (colored circles, with red indicating higher ERF and blue indicating lower ERF) and their estimated distribution (gray violin) with total (longwave and shortwave, LW + SW) ERF on the left and LW ERF on the right. (**B**) Cess climate sensitivity for X-SHiELD (red star) versus CMIP6 models (colored circles, with red indicating higher Cess sensitivity and blue indicating lower Cess sensitivity) and their estimated distribution (gray violin) with total (LW + SW) sensitivity on the left and LW sensitivity on the right.

Eq. 1 or in units of temperature by using the convention of a doubled CO_2 concentration with a radiative forcing of 3.6 W m^{-2}. The intermodel spread in radiative forcing is then suppressed to focus on the role of radiative feedbacks in determining the climate sensitivity. The Cess sensitivity omits the important role for the spatial pattern of surface temperature change in provoking more destabilizing regional feedbacks over long time scales (*22*) or projecting onto regions of more stabilizing feedbacks in recent decades (*23*). Nevertheless, this sensitivity has the virtue of simplicity and was the basis of one of the earliest GCM intercomparisons (*15*).

Figure 2B shows the Cess sensitivity, and X-SHiELD has a sensitivity of 2.31 K. Its feedback parameter λ is -1.56 W m^{-2} K^{-1} and individual years differ by 0.02 W m^{-2} K^{-1}. The mean of the CMIP6 ensemble has an incrementally larger Cess sensitivity of 2.4 K, and X-SHiELD is near the widest part of the estimated CMIP6 distribution (gray line).

The Cess sensitivity can be decomposed into LW and SW components. Here, we focus on the LW component, which is the primary stabilizing influence on climate. X-SHiELD's LW feedback parameter ($\lambda_{\mathrm{LW}} = -\Delta \mathrm{OLR}/\Delta T_s = -1.60$ W m^{-2} K^{-1}) shows that X-SHiELD's total Cess sensitivity of 2.31 K is nearly identical to the LW Cess sensitivity of 2.25 K; i.e., in this model the SW feedback is approximately neutral. Conversely, while the CMIP6 ensemble-mean total Cess feedback of 2.4 K is similar to that of X-SHiELD, the LW Cess sensitivity of 1.7 K is substantially less, and correspondingly, the CMIP6 ensemble-mean SW feedbacks are more destabilizing than in X-SHiELD. In summary, while X-SHiELD has a relatively low (compared to the CMIP6 ensemble) value for the Cess sensitivity, it has a relative high value for the LW component (that is, less stabilizing LW feedbacks) compared to the CMIP6 ensemble. The CMIP6 models are colored in Fig. 2B by their Cess sensitivity, and there is at least one GCM with low Cess sensitivity and high LW sensitivity, comparable to X-SHiELD (a dark blue dot).

Beyond a comparison to conventional climate models, it is instructive to consider how this fits with the null hypothesis that the feedbacks are primarily determined by clear-sky (non-cloud) changes and a global-mean relative humidity that is unchanged with warming. This constant relative humidity assumption was at the heart of Manabe and Weatherald's 1967 quantification of the climate sensitivity (*24*, *25*) by assuming a radiative convective equilibrium (RCE) and they found a sensitivity of 2.36 K. Contemporary single-column RCE estimates of climate sensitivity remain near 2 K (*26*–*28*). That X-SHiELD does not strongly depart from conventional GCMs, which are, in turn, broadly consistent with expectations of a constant relative humidity atmosphere with a stabilizing feedback from enhanced warming aloft in the tropics (*29*), brings our attention to X-SHiELD's atmospheric temperature and relative humidity changes under warming.

The X-SHiELD simulated time- and zonal-mean temperature change and relative humidity change are shown in Fig. 3 (A and B) for the +4 K SST perturbation simulation (with unchanged CO_2 concentration). There is enhanced warming in the tropical upper troposphere, and the warming is also amplified aloft, albeit to a lesser extent, in the extratropics (Fig. 3A). There is enhanced near-surface warming in the northern hemisphere, where the land surface temperatures can increase more than the imposed SST perturbation. (The global-mean surface air temperature warms by 4.4 K.) These features are in-line with the multi-model mean of the CMIP6 ensemble (Fig. 3C). The sign of the zonal-mean changes is robustly simulated by the individual GCMs contributing to the ensemble, as indicated by the absence of stippling. Furthermore, subsampling GCMs to two-year means has similar results (fig. S4). The upper-tropospheric enhanced warming has been a long-standing aspect of climate model analysis, both for future projections and for comparison with observations (*30*, *31*) and additional analysis of this is underway.

One of the motivations for advancing to *k*-scale storm-resolving (i.e., convection-permitting) resolution is to simultaneously explicitly simulate the large-scale and convective scale, both of which affect the mean relative humidity distribution (*32*). Examining the relative humidity in short integrations is valuable because the residence time of atmospheric water vapor is about 1 week, therefore its distribution is less sensitive to limited time averaging (fig. S5). It also has implications for global-mean climate feedbacks. The clear-sky LW feedback in conventional climate models is close to that of an increase in the specific humidity of the atmosphere with warming that leaves RH approximately unchanged (*33*, *34*).

The DYAMOND intercomparison shows that the RH distribution in the GSRM class of models agrees well with observations over short, initialized integrations (*35*). The possibility that changes in convection, such as its organization, influence the relative humidity distribution has been assessed in idealized RCE simulations of warming in the radiative convective equilibrium model intercomparison project (RCEMIP) (*36*). RCEMIP simulations span a range of mid-tropospheric relative humidity changes in response to SST

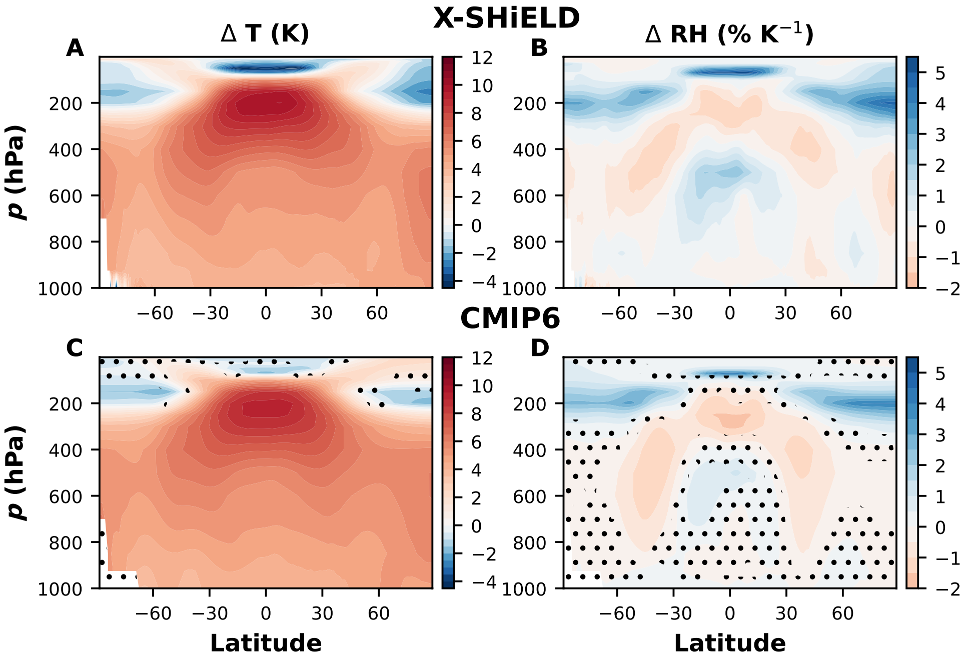

Fig. 3. Change in time- and zonal-mean temperature and relative humidity in X-SHiELD GSRM simulations compared to corresponding CMIP6 simulations in response to +4K SST. The mean change in atmospheric temperature (ΔT) (K) and relative humidity (ΔRH) (%K^{-1}) for (**A** and **B**) X-SHiELD and (**C** and **D**) the ensemble-mean of CMIP6 models. Red colors indicate decreases and blue colors indicate increases in RH, and stippling on the CMIP6 panels indicates regions where less than 75% of CMIP6 models agree on the sign of the response.

warming from about −2 to +3 % K^{-1}, with substantial associated impacts on the LW component of the radiative feedback parameter (*37*). The extent to which the divergent results among participating RCEMIP models, and relative to the modest changes in GCMs, arise from the idealized boundary conditions (which would not have direct implications for quantitative estimates of Earth's climate sensitivity) or resolving convection (which would) makes this a high priority for assessing in climate–time scale GSRM simulations.

X-SHiELD's zonal-mean relative humidity response to surface warming has local changes in the troposphere on the order of ±2 % K^{-1} (Fig. 3B). X-SHiELD has an inverted U-shaped pattern of ≈1% decreases extending from the tropical upper troposphere (near 200 hPa) downward into the subtropics and midlatitudes (Fig. 3B, red colors). Above these decreases there are regions of increased relative humidity of ≈3% that are near the climatological tropopause, where dry stratospheric air in the control simulation is becoming upper tropospheric air with a rising tropopause. These mid-to-upper troposphere changes can be characterized as an upward shift of the climatological relative humidity (*38*). This is similar to patterns in CMIP6 and across generations of GCMs (Fig. 3D) (*39*). The upward shift of an increase in relative humidity near the climatological tropopause and a decrease below is, perhaps, expected given that both parameterized and resolved convection will deepen in warmer climates. However, the detailed similarity extends to the mid-troposphere's increase in the deep tropics and the weak decrease in much of the lower troposphere.

In summary, the relative humidity response to warming is a subtle yet robust aspect of GCM-simulated changes, for which the convection-permitting RCEMIP simulations show disparate behavior. The X-SHiELD changes are in line with GCM simulations. This is highly suggestive of (i) large-scale control on the changes in relative humidity [while acknowledging that the representation of microphysical processes plays a role in determining the control RH distribution (*40*)]. This (ii) builds confidence in weak GCM-simulated changes, and, in turn, supports (iii) the now-commonplace fixed-relative humidity approach to climate feedback analysis (*33*).

DISCUSSION

Several multiple-year-long simulations of the GSRM X-SHiELD have been performed at the Cooperative Institute for Modeling the Earth System. We can subdivide the analyses of these simulations into two broad categories: examination of phenomena that cannot be investigated with conventional climate models (e.g., intense and rotating updrafts) and those that can be simulated with conventional climate models, but depend on parameterized processes and warrant careful examination in simulations with better resolved atmospheric processes. We focus on the latter here.

We have examined core aspects of the global climate's response to warming: the TOA energy balance and the temperature and relative humidity changes that underlie the basic radiative restoring of this balance when subjected to CO_2 radiative forcing. That is, the forcing and climate sensitivity of this GSRM are analyzed here and compared to conventional climate models of the CMIP6 ensemble.

One aspect of the simulated changes in X-SHiELD that departs from the CMIP6 ensemble is the effective radiative forcing. The higher-than-CMIP6 radiative forcing of CO_2 arises from both a model bias and a distinctive cloud adjustment. The control high-cloud distribution has cloud tops that are biased low in altitude and therefore have warm cloud-top temperatures, which enhances CO_2 forcing because their climatological contribution to the greenhouse effect is weaker. This also contributes to the control global-mean OLR bias (Fig. 1, left). The high-cloud adjustment is a potential mechanism of enhancing the CO_2 radiative forcing: These high-cloud changes that occur in response to increased CO_2 with unchanged SST enhance the greenhouse effect.

Compared to conventional climate models, X-SHiELD has a fairly typical Cess sensitivity of 2.3 K. The zonal-mean temperature change and relative humidity change have substantial similarities when compared to the ensemble-mean changes. The tropospheric relative humidity change is near zero in the global mean but has a zonal-mean pattern of change that is quite similar to GCMs. This stands in contrast to simulations that participated in the idealized RCEMIP intercomparison, which had substantial variations in the relative humidity response to warming and concomitantly large variations in climate sensitivity. Therefore, our results highlight the importance of large-scale controls on changes in the relative humidity distribution. This lends credibility to GCM simulations and radiative feedback assessments that take unchanged relative humidity as a reference response.

There are numerous additional avenues of follow-up research. In particular, how do other GSRMs compare to X-SHiELD? The planned third phase of DYAMOND will include year-long simulations and increased SST simulations, which will allow an examination of the dependence of the results presented here on model formulation.

MATERIALS AND METHODS

GFDL's X-SHiELD (*5*, *14*) uses the same Finite-Volume Cubed-Sphere dynamical core (FV3) as in GFDL's weather and climate models and in many other US modeling systems. At the simulation's horizontal resolution of ≈3.25 km, no deep convective parameterization is used, although there is a shallow convection parameterization. How to best handle unresolved shallow convection in *k*-scale models is still an open question and a variety of approaches are used (*9*). The X-SHiELD output analyzed here are variables that were coarsened from the native model resolution to ≈25 km online, except for fig. S2. We interpolated this coarsened 3-hourly output from X-SHiELD's 79 model levels to the standard CMIP6 pressure levels before averaging. X-SHiELD integrations have provided a "ground truth" for a machine learning approach that corrects a lower resolution version of the model (*41*, *42*), and this approach holds promise for perturbed climates (*43*).

SSTs in the control simulation are constrained to daily real-time analyses from the European Center for Medium-range Weather Forecasts (ECMWF), via a 15-day relaxation of the simulated ocean mixed layer temperature towards observed SSTs. As in prescribed SST simulations, constraining the SST via relaxation to observations can imply a global-mean energy source or sink, and ASR exceeding OLR (Fig. 1) shows that it is a sink here. Simulations were performed from late October 2019 through December 2021, with the 2019 portion of the simulation omitted from the analysis as a spin-up period. For radiative transfer, X-SHiELD uses prescribed global-mean concentrations of greenhouse gases and a climatological distribution of aerosols. The average CO_2 concentration for the analysis period is 407 ppmv, with other greenhouse gas concentrations near their contemporary values.

Figure S2 compares X-SHiELD's control simulation to active sensor estimates of tropical cloud ice (*44*–*46*). An extensive comparison of X-SHiELD and observational estimates of the atmosphere is available (*47*) or at https://extranet.gfdl.noaa.gov/~Alex.Kaltenbaugh/verification/.

Simulations of the same length were also performed with perturbed SST and/or CO_2. The SST perturbation is a uniform warming of 4 K added to the observed SST. We have also performed simulations with increased CO_2 concentration, with and without the SST warming. The perturbed CO_2 concentration is 1270 ppmv, which brings the combined perturbation experiment close to TOA equilibrium via ≈3.1× the control concentration of 407 ppmv. The perturbed CO_2 concentration was chosen based on preliminary short integrations in an attempt to have the combined perturbation 'global warming' simulation have a similar global-mean net radiation as the control simulation, although the final 2-year-long integration has a larger imbalance as stated in the main text. To compare to the $4 \times CO_2$ CMIP6 experiment, we assume a logarithmic scaling of the CO_2 concentration to estimate X-SHiELD's $4 \times CO_2$ radiative forcing: $\mathscr{F}_{4\times\mathrm{CO2}} = [\log(4)/\log(1270/407)]\mathscr{F}_{\mathrm{X-SHiELD}}$.

CMIP6 experiments are the prescribed SST AMIP simulations ("amip" experiment) with the corresponding +4 K SST perturbation ("amip-p4K" experiment) and $4 \times CO_2$ ("amip-4xCO2" experiment) simulations. The 12 CMIP6 models analyzed here are BCC-CSM2-MR, IPSL-CM6A-LR, MRI-ESM2-0, CESM2, GFDL-CM4, TaiESM1, CanESM5, CNRM-CM6-1, GISS-E2-1-G, HadGEM3-GC31-LL, MIROC6, and NorESM2-LM. The 1980–2009 climatologies are used for Figs. 2 and 3. The calculation of the Cess sensitivity uses the individual model-simulated global-mean surface air temperature change ΔT_s between the amip-p4K and amip experiments; this exceeds the imposed SST warming of 4 K because of enhanced land-surface warming. We have also examined 2008–2009 averages of CMIP6 simulations for a comparable length to the X-SHiELD integrations (figs. S1, S4, and S5).

Supplementary Materials

This PDF file includes:

Figs. S1 to S5

REFERENCES AND NOTES

1. H. Tomita, M. Satoh, A new dynamical framework of nonhydrostatic global model using the icosahedral grid. *Fluid Dyn. Res.* **34**, 357–400 (2004).
2. M. Satoh, B. Stevens, F. Judt, M. Khairoutdinov, S.-J. Lin, W. M. Putman, P. Düben, Global cloud-resolving models. *Curr. Clim. Change Rep.* **5**, 172–184 (2019).
3. Y. Tsushima, S. Iga, H. Tomita, M. Satoh, A. T. Noda, M. J. Webb, High cloud increase in a perturbed SST experiment with a global nonhydrostatic model including explicit convective processes. *J. Adv. Model. Earth Syst.* **6**, 571–585 (2014).
4. P. Narenpitak, C. S. Bretherton, M. F. Khairoutdinov, Cloud and circulation feedbacks in a near-global aquaplanet cloud-resolving model. *J. Adv. Model. Earth Syst.* **9**, 1069–1090 (2017).
5. K.-Y. Cheng, L. Harris, C. Bretherton, T. M. Merlis, M. Bolot, L. Zhou, A. Kaltenbaugh, S. Clark, S. Fueglistaler, Impact of warmer sea surface temperature on the global pattern of intense convection: Insights from a global storm resolving model. *Geophys. Res. Lett.* **49**, e2022GL099796 (2022).
6. X. Wu, Q. Fu, C. Kodama, Response of tropical overshooting deep convection to global warming based on global cloud-resolving model simulations. *Geophys. Res. Lett.* **50**, e2023GL104210 (2023).
7. J. Bao, B. Stevens, L. Kluft, C. Muller, Intensification of daily tropical precipitation extremes from more organized convection. *Sci. Adv.* **10**, eadj6801 (2024).
8. I. Guendelman, T. M. Merlis, K.-Y. Cheng, L. Harris, C. S. Bretherton, M. Bolot, L. Zhou, A. Kaltenbaugh, S. Clark, S. Fueglistaler, The precipitation response to warming and CO_2

increase: A comparison of a global storm resolving model and CMIP6 models. *Geophys. Res. Lett.* **51**, e2023GL107008 (2024).

9. B. Stevens, M. Satoh, L. Auger, J. Biercamp, C. S. Bretherton, X. Chen, P. Düben, F. Judt, M. Khairoutdinov, D. Klocke, C. Kodama, L. Kornblueh, S. J. Lin, P. Neumann, W. M. Putman, N. Röber, R. Shibuya, B. Vanniere, P. L. Vidale, N. Wedi, L. Zhou, DYAMOND: The DYnamics of the Atmospheric general circulation Modeled On Non-hydrostatic Domains. *Prog Earth Planet Sci* **6**, 61 (2019).
10. J. M. Nugent, S. M. Turbeville, C. S. Bretherton, P. N. Blossey, T. P. Ackerman, Tropical cirrus in global storm-resolving models: 1. Role of deep convection. *Earth Space Sci.* **9**, e2021EA001965 (2022).
11. S. M. Turbeville, J. M. Nugent, T. P. Ackerman, C. S. Bretherton, P. N. Blossey, Tropical cirrus in global storm-resolving models: 2. Cirrus life cycle and top-of-atmosphere radiative fluxes. *Earth Space Sci.* **9**, e2021EA001978 (2022).
12. J. Slingo, P. Bates, P. Bauer, S. Belcher, T. Palmer, G. Stephens, B. Stevens, T. Stocker, G. Teutsch, Ambitious partnership needed for reliable climate prediction. *Nat. Clim. Change* **12**, 499–503 (2022).
13. A. Gettelman, B. Fox-Kemper, G. Flato, D. Klocke, D. Stamer, B. Stevens, P. L. Vidale, Kilometre-scale modelling of the earth system: A new paradigm for climate prediction. *WMO Bulletin* **72**, 14–18 (2023).
14. L. Harris, L. Zhou, S.-J. Lin, J.-H. Chen, X. Chen, K. Gao, M. Morin, S. Rees, Y. Sun, M. Tong, B. Xiang, M. Bender, R. Benson, K. Y. Cheng, S. Clark, O. D. Elbert, A. Hazelton, J. J. Huff, A. Kaltenbaugh, Z. Liang, T. Marchok, H. H. Shin, W. Stern, GFDL SHiELD: A unified system for weather-to-seasonal prediction. *J. Adv. Model. Earth Syst.* **12**, e2020MS002223 (2020).
15. R. D. Cess, G. L. Potter, J. P. Blanchet, G. J. Boer, A. D. Del Genio, M. Déqué, V. Dymnikov, V. Galin, W. L. Gates, S. J. Ghan, J. T. Kiehl, A. A. Lacis, H. Le Treut, Z.-X. Li, X.-Z. Liang, B. J. McAvaney, V. P. Meleshko, J. F. B. Mitchell, J.-J. Morcrette, D. A. Randall, L. Rikus, E. Roeckner, J. F. Royer, U. Schlese, D. A. Sheinin, A. Slingo, A. P. Sokolov, K. E. Taylor, W. M. Washington, R. T. Wetherald, I. Yagai, M.-H. Zhang, Intercomparison and interpretation of climate feedback processes in 19 atmospheric general circulation models. *J. Geophys. Res.* **95**, 16601–16615 (1990).
16. M. A. Ringer, T. Andrews, M. J. Webb, Global-mean radiative feedbacks and forcing in atmosphere-only and coupled atmosphere-ocean climate change experiments. *Geophys. Res. Lett.* **41**, 4035–4042 (2014).
17. J. Hansen, M. Sato, R. Ruedy, L. Nazarenko, A. Lacis, G. A. Schmidt, G. Russell, I. Aleinov, M. Bauer, S. Bauer, N. Bell, B. Cairns, V. Canuto, M. Chandler, Y. Cheng, A. Del Genio, G. Faluvegi, E. Fleming, A. Friend, T. Hall, C. Jackman, M. Kelley, N. Kiang, D. Koch, J. Lean, J. Lerner, K. Lo, S. Menon, R. Miller, P. Minnis, T. Novakov, V. Oinas, J. Perlwitz, J. Perlwitz, D. Rind, A. Romanou, D. Shindell, P. Stone, S. Sun, N. Tausnev, D. Thresher, B. Wielicki, T. Wong, M. Yao, S. Zhang, Efficacy of climate forcings. *J. Geophys. Res.* **110**, D18104 (2005).
18. C. J. Smith, R. J. Kramer, G. Myhre, K. Alterskjær, W. Collins, A. Sima, O. Boucher, J.-L. Dufresne, P. Nabat, M. Michou, S. Yukimoto, J. Cole, D. Paynter, H. Shiogama, F. M. O'Connor, E. Robertson, A. Wiltshire, T. Andrews, C. Hannay, R. Miller, L. Nazarenko, A. Kirkevåg, D. Olivié, S. Fiedler, A. Lewinschal, C. Mackallah, M. Dix, R. Pincus, P. M. Forster, Effective radiative forcing and adjustments in CMIP6 models. *Atmos. Chem. Phys.* **20**, 9591–9618 (2020).
19. N. G. Loeb, D. R. Doelling, H. Wang, W. Su, C. Nguyen, J. G. Corbett, L. Liang, C. Mitrescu, F. G. Rose, S. Kato, Clouds and the earth's radiant energy system (CERES) energy balanced and filled (EBAF) top-of-atmosphere (TOA) edition-4.0 data product. *J. Climate* **31**, 895–918 (2018).
20. S. C. Sherwood, S. Bony, O. Boucher, C. Bretherton, P. M. Forster, J. M. Gregory, B. Stevens, Adjustments in the forcing-feedback framework for understanding climate change. *Bull. Am. Meteorol. Soc.* **96**, 217–228 (2015).
21. M. Bolot, L. Harris, K.-Y. Cheng, T. M. Merlis, P. Blossey, C. S. Bretherton, S. Clark, A. Kaltenbaugh, L. Zhou, S. Fueglistaler, Kilometer-scale global warming simulations and active sensors reveal changes in tropical deep convection. *NPJ Clim. Atmos. Sci.* **6**, 209 (2023).
22. M. Winton, K. Takahashi, I. M. Held, Importance of ocean heat uptake efficacy to transient climate change. *J. Climate* **23**, 2333–2344 (2010).
23. S. Fueglistaler, L. G. Silvers, The peculiar trajectory of global warming. *Geophys. Res. Lett.* **48**, e2021GL094074 (2021).
24. S. Manabe, R. T. Wetherald, Thermal equilibrium of the atmosphere with a given distribution of relative humidity. *J. Atmos. Sci.* **24**, 241–259 (1967).
25. N. Jeevanjee, I. Held, V. Ramaswamy, Manabe's radiative–convective equilibrium. *Bull. Am. Meteorol. Soc.* **103**, E2559–E2569 (2022).
26. D. D. B. Koll, T. W. Cronin, Earth's outgoing longwave radiation linear due to H_2O greenhouse effect. *Proc. Natl. Acad. Sci. U.S.A.* **115**, 10293–10298 (2018).
27. L. Kluft, S. Dacie, S. A. Buehler, H. Schmidt, B. Stevens, Re-examining the first climate models: Climate sensitivity of a modern radiative–convective equilibrium model. *J. Climate* **32**, 8111–8125 (2019).
28. B. A. McKim, N. Jeevanjee, G. K. Vallis, Joint dependence of longwave feedback on surface temperature and relative humidity. *Geophys. Res. Lett.* **48**, e2021GL094074 (2021).
29. N. Feldl, T. M. Merlis, A semi-analytical model for water vapor, temperature, and surface-albedo feedbacks in comprehensive climate models. *Geophys. Res. Lett.* **50**, e2023GL105796 (2023).
30. B. D. Santer, T. M. L. Wigley, C. Mears, F. J. Wentz, S. A. Klein, D. J. Seidel, K. E. Taylor, P. W. Thorne, M. F. Wehner, P. J. Gleckler, J. S. Boyle, W. D. Collins, K. W. Dixon, C. Doutriaux, M. Free, Q. Fu, J. E. Hansen, G. S. Jones, R. Ruedy, T. R. Karl, J. R. Lanzante, G. A. Meehl, V. Ramaswamy, G. Russell, G. A. Schmidt, Amplification of surface temperature trends and variability in the tropical atmosphere. *Science* **309**, 1551–1556 (2005).
31. S. Po-Chedley, B. D. Santer, S. Fueglistaler, M. D. Zelinka, P. J. Cameron-Smith, J. F. Painter, Q. Fu, Natural variability contributes to model–satellite differences in tropical tropospheric warming. *Proc. Natl. Acad. Sci. U.S.A.* **118**, e2020962118 (2021).
32. K. A. Emanuel, R. T. Pierrehumbert, *Clouds, Chemistry, and Climate*, vol. 35 of *NATO ASI Series I*, P. J. Crutzen, V. Ramanathan, Eds. (Springer, Berlin, 1996), pp. 17–28.
33. I. M. Held, K. M. Shell, Using relative humidity as a state variable in climate feedback analysis. *J. Climate* **25**, 2578–2582 (2012).
34. M. D. Zelinka, T. A. Myers, D. T. McCoy, S. Po-Chedley, P. M. Caldwell, P. Ceppi, S. A. Klein, K. E. Taylor, Causes of higher climate sensitivity in CMIP6 models. *Geophys. Res. Lett.* **47**, e2019GL085782 (2020).
35. T. Lang, A. K. Naumann, B. Stevens, S. A. Buehler, Tropical free-tropospheric humidity differences and their effect on the clear-sky radiation budget in global storm-resolving models. *J. Adv. Model. Earth Syst.* **13**, e2021MS002514 (2021).
36. A. A. Wing, K. A. Reed, M. Satoh, B. Stevens, S. Bony, T. Ohno, Radiative-convective equilibrium model intercomparison project. *Geosci. Model Dev.* **11**, 793–813 (2018).
37. T. Becker, A. A. Wing, Understanding the extreme spread in climate sensitivity within the radiative-convective equilibrium model intercomparison project. *J. Adv. Model. Earth Syst.* **12**, e2020MS002165 (2020).
38. M. S. Singh, P. A. O'Gorman, Upward shift of the atmospheric general circulation under global warming: Theory and simulations. *J. Climate* **25**, 8259–8276 (2012).
39. S. C. Sherwood, W. Ingram, Y. Tsushima, M. Satoh, M. Roberts, P. L. Vidale, P. A. O'Gorman, Relative humidity changes in a warmer climate. *J. Geophys. Res.* **115**, 09104 (2010).
40. T. Lang, A. K. Naumann, S. A. Buehler, B. Stevens, H. Schmidt, F., Aemisegger, on climate model in multiple climates by machine learning from 25 km resolution simulations. *J. Adv. Model. Earth Syst.* **14**, e2022MS003219 (2022).
41. C. S. Bretherton, B. Henn, A. Kwa, N. D. Brenowitz, O. Watt-Meyer, J. McGibbon, W. A. Perkins, S. K. Clark, L. Harris, Correcting coarse-grid weather and climate models by machine learning from global storm-resolving simulations. *J. Adv. Model. Earth Syst.* **14**, e2021MS002794 (2022).
42. A. Kwa, S. K. Clark, B. Henn, N. D. Brenowitz, J. McGibbon, O. Watt-Meyer, W. A. Perkins, L. Harris, C. S. Bretherton, Machine-learned climate model corrections from a global storm-resolving model: Performance across the annual cycle. *J. Adv. Model. Earth Syst.* **15**, e2022MS003400 (2023).
43. S. K. Clark, N. D. Brenowitz, B. Henn, A. Kwa, J. McGibbon, W. A. Perkins, O. Watt-Meyer, C. S. Bretherton, L. M. Harris, Correcting a 200 km resolution climate model in multiple climates by machine learning from 25 km resolution simulations. *J. Adv. Model. Earth Syst.* **14**, e2022MS003219 (2022).
44. J. Delanoë, R. J. Hogan, Combined Cloudsat-CALIPSO-MODIS retrievals of the properties of ice clouds. *J. Geophys. Res.* **115**, D400H29 (2010).
45. M. Deng, G. G. Mace, Z. Wang, H. Okamoto, Tropical composition, cloud and climate coupling experiment validation for cirrus cloud profiling retrieval using CloudSat radar and CALIPSO lidar. *J. Geophys. Res.* **115**, D00J15 (2010).
46. M. Deng, G. G. Mace, Z. Wang, R. P. Lawson, Evaluation of several A-Train ice cloud retrieval products with in situ measurements collected during the SPARTICUS campaign. *J. Appl. Meteorol. Climatol.* **52**, 1014–1030 (2013).
47. A. Kaltenbaugh, L. Harris, I. Guendelman, T. M. Merlis, K.-Y. Cheng, M. Bolot, L. Zhou, S. Clark, C. Bretherton, S. Fueglistaler, X-SHiELD model verification figures, related to: The precipitation response to warming and CO_2 increase: A comparison of a global storm resolving model and CMIP6 models, Zenodo; doi:10.5281/zenodo.10655350.
48. T. M. Merlis, Supporting data for Climate sensitivity and relative humidity changes in global storm-resolving model simulations of climate change, Zenodo; doi:10.5281/zenodo.10939276.

Acknowledgments: We thank I. Held for valuable discussions and encouragement. We thank to J. Huff and D. Klocke for helping prepare the real-time ECMWF SST analyses. **Funding:** The simulations presented here were performed using High Performance Computing resources provided by the Cooperative Institute for Modeling the Earth System, with help from the Princeton Institute for Computational Science and Engineering. This study is supported under awards NA18OAR4320123, NA19OAR0220146, and NA19OAR0220147 from the National Oceanic and Atmospheric Administration (NOAA), US Department of Commerce. This project is additionally funded by the NOAA Weather Program Office, Office of Oceanic and Atmospheric Research; and the NOAA Research Global-Nest Initiative. C.S.B. and S.K.C acknowledge funding from the Allen Institute for Artificial Intelligence. **Author contributions:** Conceptualization: T.M.M. Methodology: All authors. Investigation: T.M.M., K.-Y.C., I.G., M.B., S.K.C., and A.K. Visualization: T.M.M. and K.-Y.C. Software: L.H., K.-Y.C., L.Z., and S.K.C. Writing–original draft: T.M.M. Writing–review and editing: All authors. **Competing interests:** The authors declare that they have no competing interests. **Data and materials availability:** All data needed to evaluate the conclusions in the paper are present in the paper and/or the Supplementary Materials. The source code of X-SHiELD is available at https://github.com/NOAA-GFDL/SHiELD_build. The analysis code and data to reproduce these figures is provided in (*48*).

Submitted 13 December 2023
Accepted 22 May 2024
Published 28 June 2024
10.1126/sciadv.adn5217